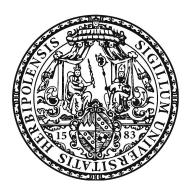**ASTRO WÜRZBURG**

# VLBI Jet Kinematics of Mrk 421 concerning the Radio Flare in 2012

Bachelors Thesis in Group of Prof. Dr. Matthias Kadler, Chair of Astronomy

## Sarah Wagner

Supervisor: Prof. Dr. Matthias Kadler
Faculty for Physics and Astronomy
Julius-Masimilians-Universität Würzburg

Würzburg, May 2018

# Abstract

Markarian 421 (Mrk 421) belongs to the most observed objects in the universe. With a redshift of $z = 0.031$ the active galactic nucleus is one of the nearest BL Lac objects to the solar system. Due to the fact that the first extragalactig TeV photons originated from this source (see Punch et al. 1992), many further observations were initiated. Hereby, for instance, a radio flare was detected in September 2012 (see Hovatta et al. 2012). This flare is analyzed at 15 GHz in Richards et al. (2013) where it is declared to be the most powerful increase in intensity observed in the radio regime of any blazar.

The scientific interest in this flare is particularly big because of an additional $\gamma$-Flare that occured circa 40 days earlier (see D'Ammando & Orienti 2012 and Hovatta et al. 2015). As pointed out in Jorstad et al. (2001) such flaring behaviour indicates the ejection of a new radio component into the jet. This can be varified in analysis of the VLBI jet structure of the jet. Hence, in this work data of the Boston University Blazar Monitoring Program is used to study the VLBI jet structure of Mrk 421 before, throughout, and after the peroid of the multiwavelenght flaring. This includes 15 epochs from January 2012 to July 2013 observed with radio interferometry of the Very Long Baseline Array (VLBA) at 43 GHz. The hereby obtained, so called complex visibilities are analyzed in difmap. This program allows to utilize the widely accepted method of hybrid imaging and model-fitting where the brightness distribution of the source is modeled with point sources and Gaussian components respectively.

The key question is whether the radio flare of Mrk 421 in September 2012 caused changes in the VLBI structure of the source at 43 GHz. Based on the results in this work that has to be neglected. No significant change could be noticed in 15 epochs from January 2012 to July 2013 in the proper jet motion with the mentioned mehtods. It has to be noted that the procedure itself reaches its limits for this source. While at other frequencies and for different sources multible components can be detected, this study only allows to identify one component apart from the bright core. Even this component is uncertain in some epochs. Similar results can be shown in other studies like Blasi et al. (2013) and Jorstad et al. (2017). Often it is not clarified how vague the utilized method can be.

# Zusammenfassung

Markarian 421 (Mrk 421) gehört zu den meist beobachtetsten Objekten im Universum. Mit einer Rotverschiebung von nur $z = 0,031$ ist die aktive Galaxie eines der nähsten BL Lac Objekte in unserer Umgebung. Als die ersten extragalaktischen TeV Photonen dieser Quelle zugeschrieben wurden (siehe Punch et al. 1992), wurde großes Interesse für weitere Beobachtungen geweckt. So wurde beispielsweise im September 2012 ein Radio-Flare entdeckt (siehe Hovatta et al. 2012). Die darauf basierende Studie in Richards et al. (2013) zeigt, dass es sich hierbei um den extremsten Helligkeitsanstieg handelt, der je im Radiobereich eines Blazars beobachtet wurde.

Das wissenschaftliche Interesse an diesem Flare wird neben seiner Einzigartigkeit durch einen vorhergehenden $\gamma$-Flare (siehe D'Ammando & Orienti 2012 und Hovatta et al. 2015) verstärkt. Die These, dass solche $\gamma$-Flares das Erscheinen einer neuen Radio Komponente im Jet ankündigen (siehe Jorstad et al. 2001), motiviert die genaue Untersuchung der Jet Struktur. Hierfür werden die Radiointerferometriedaten vom Boston University Blazar Monitoring Program herangezogen. Auf der zugehörigen Website werden die circa monatlichen Beobachtungen mit dem Very Long Baseline Array bei 43 GHz bereitgestellt. Im Rahmen dieser Arbeit werden jene sogenannten "complex visibilities" durch durch die breit anerkannten Methoden "hybrid imaging" und "model-fitting" in difmap analysiert. Das bedeutet, dass die Helligkeit der beobachteten Quelle mit einem Modell nachgestellt wird. Während bei der ersten Methode Punktquellen zugrunde liegen, baut die zweite Methode auf Helligkeitspunkten gemäß einer Gaußverteilung auf, die die Radio Komponenten repräsentieren sollten.

Kernfrage ist also, ob nach dem Radio Flare von Mrk 421 im September 2012 Veränderungen der VLBI Jet Struktur bei 43 GHz, wie beispielsweise eine neue Komponente, erkennbar sind. In den 15 Epochen von Januar 2012 bis Juli 2013 konnten mit den genannten Methoden in dieser Studie keine Veränderungen festgestellt werden. Hierbei ist jedoch an zu merken, dass die Vorgehensweise bei dieser Quelle an ihre Grenzen stößt. Während bei anderen Frequenzen und anderen Quellen mehrere deutliche Komponenten erkennbar sind, lässt sich hier abgesehen vom hellen Kern nur eine Komponente identifizieren. Selbst diese ist nicht immer eindeutig erkennbar. Ein ähnliches Ergebnis zeigen andere Studien wie Blasi et al. (2013) und Jorstad et al. (2017). Oft wird nicht deutlich wie vage die Modellinterpretationen sind.

# Contents

# 1 Scientific Context

The source Markarian 421 (Mrk421) at RA = $11^h04^m27.314^s$ and DEC = $+38°12'31.80''$ belongs to the most studied blazars in the universe. With a comparably small redshift of z=0.031 and the first extragalactic TeV emission (see Punch et al. 1992) many multi wavelength campaigns have been conducted in order to study this source. Based on those observations, Mrk 421 can be classified as high synchrotron peaked BL Lac with variability across the electromagnetic spectrum.

## 1.1 Classification

### 1.1.1 AGN

Mrk 421 is a particular type of active galactic nuclei (AGN) which is the very luminous inner part of an active galaxy. Those can be divided in radio loud and radio quiet AGN based on the ratio of radio ($5\,\mathsf{GHz}$) and optical (B-band) flux. As introduced in Kellermann et al. (1989), an AGN is radio loud if that ratio is bigger than 10. In the following, only radio loud objects will be discussed. This includes 15-20% of all AGN. According to the unification scheme in Urry & Padovani (1995), sources that were thought to be different physical objects due to distinct features like narrow and broad emission lines, are infact different views of the same type of source. The widely accepted structure of such an object is an AGN as shown in Fig. 1.1[1].

---

[1] Figure is not to scale: typical parameters according to Urry & Padovani (1995): accretion disc $1 - 30 \cdot 10^{14}\,\mathsf{cm}$, broad-line region $2 - 20 \cdot 10^{16}\,\mathsf{cm}$, inner radius of torus $10^{17}\,\mathsf{cm}$, narrow-line region $10^{18} - 10^{20}\,\mathsf{cm}$, radio jets $10^{17} - 10^{24}\,\mathsf{cm}$
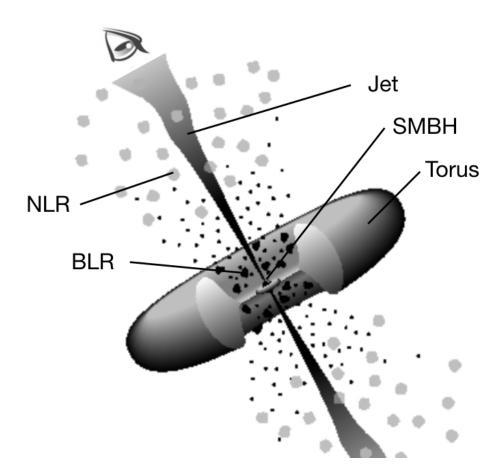
**Figure 1.1:** Widely accepted unscaled AGN scheme according to Urry & Padovani (1995). Characteristics of narrow line region (NLR), broad line region (BLR) and torus cause various features for different angels of view as explained in the text. If the line of sight is close to the jet axis, as indicated with the eye, the AGN is called blazar.

A supermassive black hole (SMBH) is expected to be in the center of every AGN as shown in Fig. 1.1. Due to its big mass it causes gas and dust from the galaxy to fall towards its center. The particles thereby lose angular momentum in consequence of viscous or turbulent processes. Shakura & Sunyaev (1973) state that this angular momentum is transported outwards which causes the material to form an accretion disc that can also be seen in Fig. 1.1. The extreme movement within this disc induces friction and therefore heats up the accretion disc which cools via black body radiation. This spectrum is dependent on the matter inflow and most powerful in the optical and ultra-violet (UV) for AGN discs. Additionally, optical radiation is emitted where material of

the colder, more outward region of the disc is excited by the inner radiation.

The optical and UV spectrum contain broad emission lines. Those are emitted in clouds of the so called broad line region (BLR) sketched as black dots in Fig. 1.1. Since those clouds move rapidly, the emission lines are widened due to Doppler-broadening. Even though these broad emission regions are expected to exist in every AGN, the resulting lines are not always observed. Depending on the inclination angle of the AGN to the line of sight, the broad emission region can be hidden by the opaque torus of gas and dust enclosing the accretion disc. In this case, prominently narrow emission lines that emerge in rather slow clouds from the so called narrow line region (NLR), depicted with grey blobs in Fig. 1.1, are observed.

Radio loud AGN typically feature bipolar jets perpendicular to the disc up to Mpc - scales. The exact acceleration mechanisms that causes such a highly collimated stream of energetic particles are still to be observed. Indications for this are provided by Blandford & Znajek (1977) discussing the extraction of electromagnetic energy from the rotation energy of the SMBH and Blandford & Payne (1982) describing accretion disc wind-driven jets.

The above clarifies that the observed features are subject to the angle of view even for the same physical object. Since this has not been known in the past, the different appearences lead to different names that are listed in Urry & Padovani (1995). Since Mrk 421 has been classified as blazar and further as BL Lacertae (BL Lac) object only those sources will be discussed here. In this case, the line of sight is closely aligned with the direction of the jet as illustrated in Fig. 1.1. This means, when observing from Earth we are looking almost directly into the jet. The survey of Urry et al. (2000) shows that the host galaxy of such objects is usually a luminous elliptical.

## 1.1.2 Blazar

In general, the inclination angle of an AGN, illustrated in Fig. 1.1, classifies an object as blazar. In observations, this line of sight is verified in the spectral energy distribution (SED) that should show a double hump. In such diagrams, the flux density $f$ is plotted in dependency of the frequency $\nu$. Very often the $f$-axis of flux density is multiplied with $\nu$. In this case, the integral of the fitted graph yields the total emitted power of the object within the integrated frequency band.
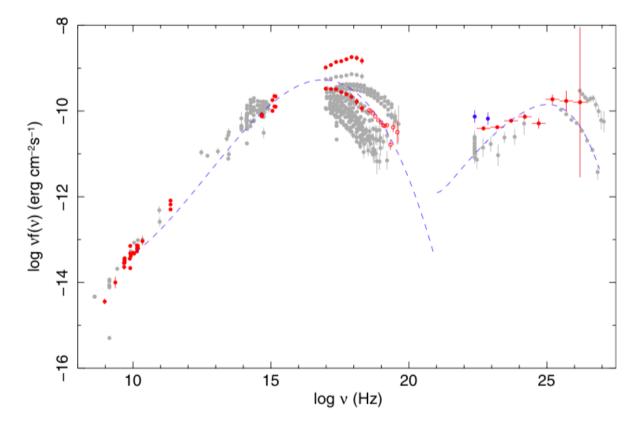
**Figure 1.2:** Spectral Energy Distribution (SED) of Mrk 421 as plotted in Abdo et al. (2010) based on Fermi $\gamma$-ray spectra with Swift, radio, infra-red, optical, and other hard X-ray/$\gamma$-ray data. Synchrotron and inverse Compton peak are fitted with a third-degree polynomial.

A so called broadband continuum is expected for all radio-loud AGN. This implicates that the graph does not have the shape of a blackbody radiation curve as, for instance, in stars caused by thermal radiation. The SED graph of an AGN is comparably flat as represented in the power law $f \propto \nu^{-\alpha}$ of flux density $f$ and frequency $\nu$ with $\alpha \approx 1$. Fig. 1.2 shows such a flat SED of Mrk 421 from Abdo et al. (2010) where the two humps are fitted with a simple third-degree polynomial. The explanation for this particular shape will be given in Sect. 1.2 and allows to classify the source as blazar and furthermore as high synchrotron peaked (HSP) BL Lac object.

## 1.1.3 BL Lac object

The radio-loud blazars can be divided further in two sub-classes according to the presence of emission features. As summarized in Urry & Padovani (1995), all blazars with emission lines can be referred to as Flat Spectrum Radio Quasars (FSRQ). If there are no emission lines detectable the object is classified as BL Lacacertae object (BL Lac).

This tracks back to the first observed source of that kind: BL Lac. While it was first thought to be a star, Schmitt (1968) identified the object as radio source. Further observations revealed similar sources, leading to the conclusion that "BL Lacs" are an own kind of source as Strittmatter et al. (1972) summarize. Vermeulen et al. (1995), however, show that even the object used for classification of those blazars itself sometimes shows emission lines.

Mrk 421 does not show emission lines, as shown by Abdo et al. (2010), and is therefore classified as BL Lac object. Urry & Padovani (1995) list further typical features of BL Lac objects, such as very rapid variability, high and variable polarization, high brightness temperatures, and sometimes superluminal velocities of compact radio cores (see Sect. 1.3 for latter). Concordant with the above classification, Gaidos et al. (1996) report two very rapid TeV outbursts of Mrk 421. The measured variability on timescales of hours is dramatic even for comparable objects. In fact, Mrk 421 was the first extragalactic source of which TeV emission was detected (see Punch et al. 1992).

A further specification is that Mrk 421 is a high synchrotron peaked (HSP) blazar. As defined in Abdo et al. (2010), this means that the peak of the first hump, caused by synchrotron radiation, reaches UV or higher energies ($\nu_{peak} \gtrapprox 10^{15}\,\mathsf{Hz}$). In comparison to the low synchrotron peaked objects ($\nu_{peak} \lessapprox 10^{14}\,\mathsf{Hz}$) the emitting particles must be accelerated to higher energies.

To sum up, Mrk 421 is a high-synchrotron-peaked blazar that is interesting for many reasons. The outstanding variability and the small distance to the object motivated many observations. One example for those is the Boston Universtiy Blazar monitoring program (see Sect. 2.3), where measurements of Mrk 421 at 43 $\mathsf{GHz}$ are conducted roughly once a month. Thereby, the period around the exceptional radio flare in September 2012 (see Richards et al. 2013) is covered. That data will be analyzed in this study in order to find out whether the radio flare had significant impacts on the structure of the VLBI-jet.

## 1.2 Radiative processes

As already mentioned and explained in detail in Shakura & Sunyaev (1973), parts of the active galactic nucleus emit thermal radiation from the optical to UV band. Nevertheless, the clear difference to a black body spectrum, as in the two humps seen in Fig. 1.2, manifests that the spectrum of a blazar is dominated by non-thermal radiation. One of the humps is located at low energies (UV through X-rays) and another one at higher energies (X-rays through $\gamma$-rays). The reason for the first peak is synchrotron emission according to Abdo et al. (2011). The second one can be described by inverse Compton-processes in leptonic models. Additionaly different hardronic processes, as shown in Mannheim (1993), can influence the shape of the SED. As that radiation is thought to emerge in the jet which is of particular interest for this study, the essential principles are outlined here according to Rybicki & Lightman (1986).

The first bump in the low-frequency range is due to synchrotron radiation which is caused by a charged particle moving in a constant magnetic field. Considering an electron with elementary charge $e$, velocity $\boldsymbol{v}$ and mass $m_e$ in a magnetic field $\boldsymbol{B}$ the Lorentz-Force causes the equation of motion of that particle to be

$$\frac{d}{dt}\gamma m_e \boldsymbol{v} = \frac{e}{c}\boldsymbol{v} \times \boldsymbol{B} \tag{1.2.1}$$

with the Lorentz factor $\gamma = \frac{1}{\sqrt{1-\beta^2}}$ and $\beta = \frac{v}{c}$. This results in a helical motion of the particle around the magnetic field lines with the frequency $\omega_B$ based on the Gyro frequency $\omega_L$[2].

$$\omega_B = \frac{1}{\gamma}\frac{eB}{m_e c} \qquad \omega_L = \frac{eB}{m_e c} \tag{1.2.2}$$

Naturally an accelerated particle like this emits radiation. Rybicki & Lightman (1986) derive the emitted power for an isotropic velocity distribution to be:

$$P = \frac{4}{3}\sigma_T c \beta^2 \gamma^2 U_B \tag{1.2.3}$$

with the magnetic field energy distribution $U_B$ and the Thomson cross section $\sigma_T$. Due to the fact that $\sigma_T$ scales with $m^{-2}$ it is reasonable to only consider leptons and neglect

---

[2] $\omega_L$ is also called Lamor or Cyclotron frequency

heavier hardrons for a first approximation.

The explained radiation process is shown in Fig. 1.3 for two points (1 and 2) with blue emission cones. This illustrates that the observer sees a pulse of radiation confined to a time interval much smaller than the gyration period. The particle passes point 1 (2) at the time $t_1$ ($t_2$) and causes radiation that is seen at time $t_1^O$ ($t_2^O$) at the observers position. This means the particle takes the time $\Delta t = t_2 - t_1$ to travel along the trajectory from point 1 to point 2. Due to the fact that light travels faster than this particle the observer notices the difference $\Delta t^O$ according to:

$$\Delta t^O = t_2^O - t_1^O = \left(1 - \frac{v}{c}\right)\Delta t = (1 - \beta)\Delta t \qquad (1.2.4)$$

The approximation $\beta \approx 1$ now allows to set $(1 - \beta) \approx 1/2\gamma$ which can be utilize in order to define the characteristic frequency of the radiation $\omega_c = 1/\Delta t^O$ to be:

$$\omega_c = 2\pi\nu_c = \gamma^2\omega_L = 2\pi\gamma^2\nu_L = \frac{E}{m_e c}^2 \frac{eB}{m_e c} \qquad (1.2.5)$$

As the spectrum of a single electron has a strong peak at that frequency it is reasonable to assume only one emission frequency in approximation.

Considering not only one electron but many with various energies the emitted power spectrum is expressed by

$$P_\nu = \int_1^\infty = P_\nu(\gamma)n(\gamma)d\gamma \qquad (1.2.6)$$

where $n(\gamma)$ represents the distribution function of number of electrons at a specific energy. Taking into account non thermal synchrotron radiation $n(\gamma)$ is described by a power law such as:

$$n(\gamma)d\gamma = n_o\gamma^{-p}d\gamma \qquad (1.2.7)$$

In order to eventually derive the SED of such an electron population the spectral shape $\Phi(\gamma)$ with $\int \Phi_\nu(\gamma)d\nu = 1$ is introduced. In a first step the spectral energy distribution $P_\nu(\gamma)$ for one electron with total energy $E = \gamma m_e c^2$ can be expressed with Eq.1.2.3 and the spectral shape by:

$$P_\nu(\gamma) = \frac{4}{3}\sigma_T c\beta^2\gamma^2 U_B\Phi_\nu(\gamma) \qquad (1.2.8)$$

As elucidated before the radiation of an electron can be approximated with one peak at
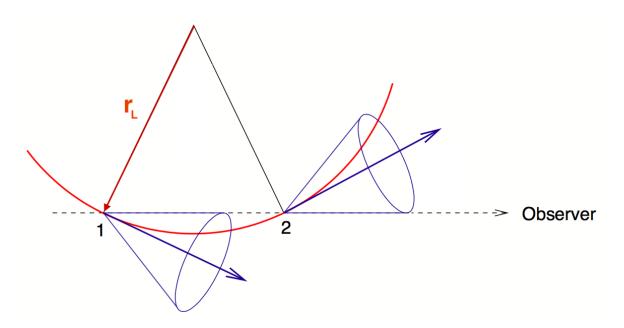
**Figure 1.3:** Emission cones (blue) representing radiation at two distinct points (1 and 2) along the trajectory of the particle (red) defined by the Lamor radius $r_L$. (Figure adapted from Kadler 2017)

the characteristic frequency $\nu_c$. This is expressed in the spectral shape function as Dirac $\delta$ distribution:

$$\Phi_\nu(\gamma) \propto \delta(\nu - \nu_c) = \delta(\nu - \gamma^2 \nu_L) \tag{1.2.9}$$

Applying this to Equ.1.2.6 yields the final power spectrum of a electron distribution at different Energies:

$$P_\nu = \int_1^\infty = \frac{4}{3}\sigma_T c\beta^2\gamma^2 U_B \delta(\nu - \gamma^2\nu_L)\, n_o\gamma^{-p}d\gamma$$

$$P_\nu = \frac{2}{3}\sigma_T cU_B \frac{1}{\nu_L}\left(\frac{\nu}{\nu_L}\right)^{-(p-1)/2} \tag{1.2.10}$$

The second form was obtained for $\beta \approx 1$ by substituting $\nu' = \gamma^2\nu_L$ and proves that a electron power-law distribution emits a spectrum following a power-law. The composition of this powerlaw is illustrated in Fig. 1.4. Due to the fact that the electrons with the highest energy radiate their energy the fastest, the spectrum steepens at high frequencies. Furthermore the shape of the SED changes if the radiation does not take
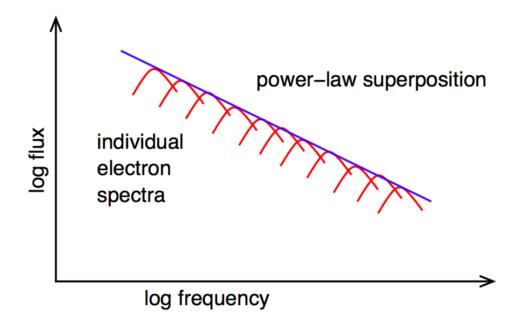
**Figure 1.4:** Spectral energy distribution of one electron power-law distribution (blue) composed by various characteristic single pulses (red). (Figure adapted from Kadler 2017)

place in transparent interior which was assumed up to now. This is taken into account with the optical depth $\tau_\nu$ that is the smaller the more transparent or optically thin the medium is calculated in dependence of traveled distance $s$ of the light and the absorption coefficient $a_\nu$.

$$\tau_\nu(s) = \int_{s_0}^{s} a_\nu(s')ds' \qquad (1.2.11)$$

In optical thick interior ($\tau_\nu > 1$) chances are high that a photon emitted via synchrotron radiation interacts with another relativistic electron of the distribution. The photon hereby gets absorbed which is called synchrotron self absorption. This causes a decrease according to $P_\nu \propto \nu^{5/2}$ as derived in Rybicki & Lightman (1986) and illustrated in the final SED of a power-law electron distribution in Fig. 1.5. It is widely accepted that the low frequency bump in the SED of AGNs is caused by the outlined mechanisms.

The reason for the second hump is still discussed. Various arguments account for inverse Compton scattering. This so called Synchrotron Self-Compton (SSC) model, explained in Marscher & Gear (1985), states that the population of relativistic electrons interacts again with the synchrotron radiation produced by themselves. The photons
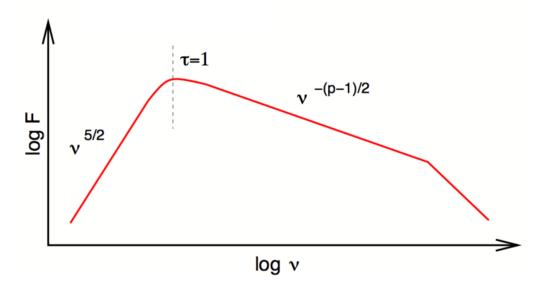
**Figure 1.5:** Total SED of a electron power-law distribution. (Figure adapted from Kadler 2017)

hereby gain energy from the electrons in scattering processes. The electron transfers most of its energy to the photon, often boosting it into the gamma regime, which could explain the second hump as illustrated in Paggi et al. (2009).

In addition to this radiation processes of leptons the same can take place for hardrons, as pointed out in Mannheim (1993). This study shows explicitly for Mrk 421 that such processes fit the observed SED.

As it is caused by highly relativistic electrons, the radiation appears beamed when observing it in line of sight to wards the jet. Cohen et al. (2007) point out that the apparent transverse speed $\beta_{app}$ and the apparent luminosity $L_0$ for a beamed radio jet differ from the intrinsic quantities, which are the Lorentz factor $\gamma = \frac{1}{\sqrt{1-(v/c)^2}}$ and the intrinsic luminosity $L_0$. For transition of those quantities the Doppler factor

$$\delta = \frac{1}{\gamma(1 - \beta \, cos\theta)} \tag{1.2.12}$$

is introduced with the angle to the line of sight $\theta$ and $\beta_{app} = \frac{\beta sin(\theta)}{1-\beta cos(\theta)}$. The boosting causes the emitted radiation to be firstly blue shifted due to Doppler shifting and secondly gets amplified, which is important to consider when analyzing BL Lac objects.
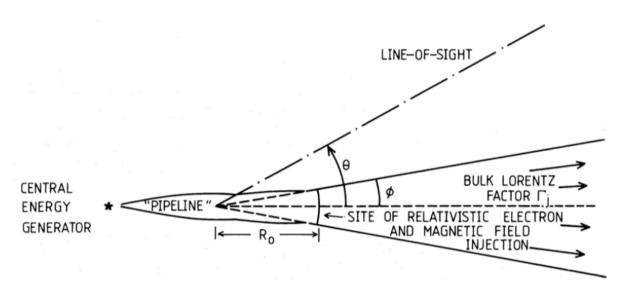
**Figure 1.6:** Conical structure for shock-in-jet model. Vertex of the cone with opening
angle $\phi$ does not have to be equal to central engine. Plasma gets injected at $R_0$ and
propagates as described by the Lorentz factor $\Gamma_j$. (Figure adapted from Marscher &
Gear 1985)

## 1.3 Jet structure

In order to reproduce the millimeter to infrared flare of 3C 273 in 1983, Marscher & Gear
(1985) developed a model of such a relativistic jet. The so-called shock-in-jet model that
they came up with was found to be very successful in qualitatively reproducing the event.
It assumes a jet structure as illustrated in Fig. 1.6. The jet is described as a cone with
the constant opening angle $\phi$. Hereby, the vertex of the cone does not necessarily rep-
resent the central engine (SMBH) of the object, which might be linked though a not
further defined "pipeline" or 'nozzle". This is, however, not physically relevant for the
description. Relativistic electrons and magnetic field are injected in an axial distance
$R_0$ from the vertex. From here on the plasma flows steadily outward with a relativistic
speed that is defined by the Lorentz factor $\Gamma_j$. The line of sight is determined by the
angle $\theta$.

Assuming that the jet flow is adiabatic, Marscher & Gear (1985) show that the be-
havior of 3C 273 can be reproduced with variations of $R_0$, for instance. The necessary
consequence of such changes in flow parameters (resulting in an increase in pressure of
the jet flow) is the formation of shock waves. This shock model represent the physics

of the flare in early 1983 very well according to that study. It further allows to explain superluminal knots on the VLBI map that have been found but not yet explained before as shocked regions in the relativistic jet. The overview of mm-VLBI studies given in Boccardi et al. (2017) shows that most of the jets can be well modeled with such knots. Therefore, also this study adapts the shock-in-jet model for interpretation of the radio components.

## 1.4 Radio Flare in September 2012

### 1.4.1 Why this flare was extraordinary

As pointed out Mrk 421 is a very interesing HSP BL Lac object. Various flares were observed in different wavelengths throughout the years. This study will focus on the radio flare in September 2012 that is reported in Hovatta et al. (2012). Despite the fact that Mrk is very variable in the high-energie regime, the radio regime of the source has been rather stable (see Fig. 1 in Richards et al. 2013). This tame radio behaviour has been observed in many other BL Lac sources as well (see Ackermann et al. 2011). They do still show flares as Hovatta et al. (2009) presents. In that study about 500 flares of 80 blazars were analyzed at 22 and 37 GHz. A flare in general is defined as the rapid increase of flux density from a particular source. The study yields a medain doubling time of about 60 days and never below 9 days for those flares. Comparing this to the doubling time of only 9 days at 15 GHz in the flare of Hovatta et al. (2012) shows that this is an exceptional radio flare. Since the higher frequency yields higher resolution the 22 GHz and 37 GHz data represent regions closer to the core. In that area the flares are expected to be faster and stronger. Yet even the 15 GHz flare in 2012 is more rapid than all the rest included in the study of Hovatta et al. (2009).

In addition to that there was also flaring in the $\gamma$-regime as reported in D'Ammando & Orienti (2012). Hovatta et al. (2015) show that this event consisted of two peaks each of which could be physically connected to the radio flare. Jorstad et al. (2001) describe a connection between $\gamma$-ray flares and an ejection of a new superluminal component into the VLBI jet. The identification of such a new component would support that theory.

## 1.4.2 Analysis in 15 GHz

Richards et al. (2013) analyse this exceptional radio flare at 15 GHz. It is stated that the flare was seen in almost all wavelengths from 2.6 GHz to 142 GHz. This is illustrated in the light curve in Fig. 1.7 where the overall flux of the source is plotted against time. It is important to note that not all wavelengths are as well covered with data points as the 15 GHz set. For 43 GHz for instance there are only two measurements, that are highlighted with purple lines in the plot. Based on those there is no evidence for the flare in that wavelength. This motivates to study the behaviour at 43 GHz in order to analyze whether the flare was also visible there. The corresponding light curve will be analyzed in Sect. 4.3.

Since the flare is clearly seen in the 15 GHz data of Richards et al. (2013) it could be possible to see changes in the jet structure. The reason for flares like this is not clear. It could be possible that a new component was injected into the jet (see Sect. 1.3) causing the object to increase its brightness rapidly. According to the 15 GHz data, however, no new component could be found within the jet. A subtraction of the intensity in April (before the flare) from the intensity in October (after the flare) only yields a difference of intensity in the core region as can be verified in Fig. 4 of Richards et al. (2013). No structural changes can be found within the jet. According to Fig. 6 of the same paper there are 5 almost stationary components just as before the flare.

Based on this paper there are two possibilities for the structure of the jet:

- either the structure of the jet and its components did not change

- or the changes and the suspected new component could not be resolved at 15 GHz.

Therefore, it is crucial to analyze available data in higher resolution in order to get a deeper understanding of the exceptional radio flare in 2012.

## 1.4.3 Related observations in 43 GHz

The Boston University Blazar Monitoring Program (see Sect. 2.3) provides long term observation data of Mrk 421 at 43 GHz. For the reasons pointed out above the data between January 2012 and July 2013 is used in this work to gain knowledge about the innermost region of the BL Lac throughout the period of the flare.
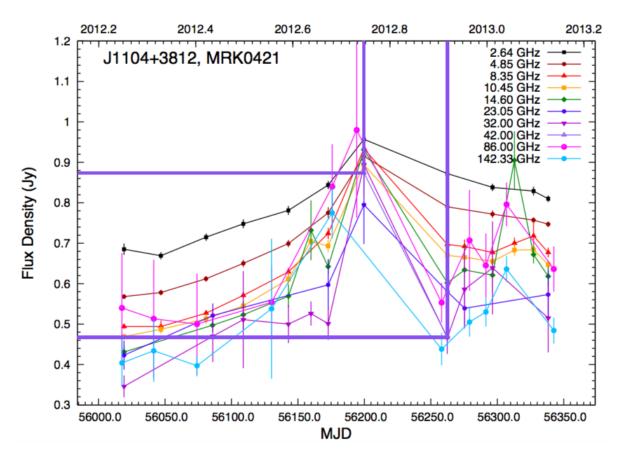
**Figure 1.7:** Light curve of Mrk 421 in multiple radio wavelengths as shown in Richards et al. (2013) based on the overall intensities. In this set of data the flare in September and a pre-flare in August 2012 can be seen in almost every wavelength. Only two data points are available for 43 GHz as illustrated with purple lines.

The same observation program provided data for 2011. This period was interpreted in Blasi et al. (2013). A model of five to six components is suggested whereby four rather stationary components could be identified in every epoch. Those results will be compared and discussed in detail along with the results of this work in Chap. 4.

Additionaly the models for Mrk 421 found in Jorstad et al. (2017) are included in the discussion. In that study 12 BL Lac objects were analyzed at 43 GHz concerning their jet kinematics throughout several years. Thereby no significant features were found in Mrk 421 regarding the radio flare in September 2012. That work, however, did not focus on Mrk 421 and only includes data up to January 2013 while this study will include

observations up to July 2013.

To sum up the main question of this study is whether the extraordinary radio flare of the BL Lac Mrk 421 in September 2012 is seen in its jet structure at 43 GHz. The data is provided from Boston University Blazar Monitoring Program and covers the period from January 2012 up to July 2013 with 15 observations. The results will be compared with the interpretation of the same data up to January 2013 in Jorstad et al. (2017) and earlier data of 2011 shown in Blasi et al. (2013)
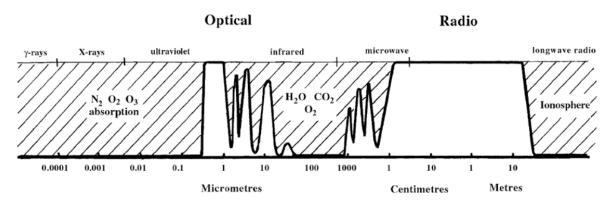
# 2 Radio Astronomy

Due to the fact that extra galactic objects such as AGNs are very far away it is crucial to achieve the best possible resolution when observing them. For the innermost region of the jet structure, as it is of interest for this study, a resolution of milliarcseconds or below is necessary. This is only achieved with radio interferometry as explained in the following.

## 2.1 Radio Observations

The radio regime reaches from wavelengths of a few millimeter to a few meter. As any other electromagnetic radiation radio waves are affected by the phenomena of reflection, refraction, diffraction, absorption, polarization, and scattering. At low frequencies the waves travel beyond the horizon as surface waves which follow the contour of the earth. Therefore those radio waves are very useful for communication worldwide. Bell Laboratories for instance used them in the 1930s to operate a transatlantic telephone from New York to London. Occasionally having difficulties with the signal the company assigned Karl Jansky to detect disturbances. Besides nearby and distant thunderstorms there was a "faint steady hiss of unknown origin". The unsuspecting scientist detected the first radio waves from space. (from Verschuur 2007)

This serendipity was only possible because the atmosphere of the earth is transparent for radio waves. Fig. 2.1 from Burke & Graham-Smith (2010) illustrates this so called radio window. The y-axis represents the percentage of intensity that reaches the terrestrial ground depending on the wavelength depicted along the x-axis. While radiation with $\lambda > 30\,\mathrm{m}$ is reflected by the ionosphere and molecules like $H_2O, CO_2$ and $O_2$ absorb waves with $\lambda < 1\,\mathrm{mm}$, radiation within this frame is observable from earth. Therefore, radio astronomy can be conducted with terrestrial telescopes.

**Figure 2.1:** Transparency in atmosphere of the earth for electromagnetic radiation of different wavelengths. Aside of the optical regime a "window" is only present for radio waves. (Figure adapted from Burke & Graham-Smith 2010)

While Burke & Graham-Smith (2010) provide a basic introduction to radio astronomy Taylor et al. (1999) include a chapter by B.G. Clark that offers a very different, theoretical approach. The focus is not laid on the measurement process itself but on the basic measured quantity from the source. This approach will be outlined in the following.

Starting point is is an astronomical object at location $\boldsymbol{R}$ causing a time-variable electric field $\boldsymbol{E}(\boldsymbol{R}, t)$ due to a not further classified phenomenon. As described by the Maxwell's equations this causes propagating electromagnetic waves. Hence the electric field can be measured at another location $\boldsymbol{r}$ to be $\boldsymbol{E}(\boldsymbol{r}, t)$. This is pictured in Fig. 2.2 a).

Considering a finite time interval of variation, eliminates the direct time dependency. This is achieved by describing the magnitude of the field with the real part of the sum of the Fourier series where the only time varying functions are simple exponentials. Bearing in mind the linearity of the Maxwell's equations in the following, justifies that the coefficients of this Fourier series are sufficient for further discussion. Those so called quasi-monochromatic components of the electric field will be denoted with $\boldsymbol{E}_\nu(\boldsymbol{R})$ and are complex quantities. $\boldsymbol{E}_\nu(\boldsymbol{r})$ at a potential observer is influenced by $\boldsymbol{E}_\nu(\boldsymbol{R})$ at the source as described with the propagator $P_\nu$ according to:

$$\boldsymbol{E}_\nu(\boldsymbol{r}) = \iiint P_\nu(\boldsymbol{R}, \boldsymbol{r})\, \boldsymbol{E}_\nu(\boldsymbol{R})\, dx\, dy\, dz \qquad (2.1.1)$$

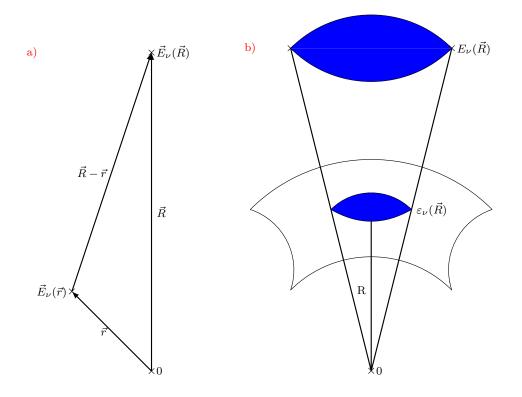The following assumptions allow simplifications for this parameter.

**Figure 2.2:** *a)* Considered source at $\boldsymbol{R}$ emitting $E_\nu(\boldsymbol{R})$ observed at $\boldsymbol{r}$ to be $E_\nu(\boldsymbol{r})$.
*b)* Illustration of second assumption: Brightness distribution on celestial spherical surface that incorporates information about source can be shifted. Space inbetween the spheres is thought to be empty. (Figure adapted from Burd 2017)

- The electric field is considered to be a scalar field neglecting any possible polarization phenomena.

- Due to the large distance of astronomical objects, no three dimensional but only a surface brightness can be derived. This surface brightness is distributed on a spherical celestial surface that can be shifted with equivalent information from $E_\nu(\boldsymbol{R})$ to $\varepsilon_\nu(\boldsymbol{R}*)$ as illustrated in Fig. 2.2 b).

- The space in between those two surfaces is assumed to be empty. In consequence the propagator reads $\frac{e^{2\pi i \nu |\boldsymbol{R}-\boldsymbol{r}|/c}}{|\boldsymbol{R}-\boldsymbol{r}|}$ due to the Huygens' Principle.

Taking those into account for Eq. 2.1.1 yields

$$E_\nu(\boldsymbol{r}) = \int \varepsilon_\nu(\boldsymbol{R}) \, \frac{e^{2\pi i\nu|\boldsymbol{R}-\boldsymbol{r}/c}}{|\boldsymbol{R}-\boldsymbol{r}|} \, dS \qquad (2.1.2)$$

with the element of surface area $dS$ on the sphere. Eq. 2.1.2 represents the impact of all electromagnetic radiating sources on the quasi-monochromatic component at $\boldsymbol{r}$ for a frequency $\nu$. In this formalism Eq. 2.1.2 describes all information concerning the electric field obtainable from an astronomic source. This is electric field can be measured by radio telescopes.

## 2.2 Very Long Baseline Interferometry

### 2.2.1 Motivation for Radio Interferometry

As pointed out in Chap. 1 especially the brightness distribution of the small core region of a blazar like Mrk 421 is very important. This requires an angular resolution below milliarcseconds. The Reyleigh criterion limits the angular resolution $\Theta$ in dependency of the telescope diameter $D$ and the observing wavelength $\lambda$ in zeroth order by:

$$\Theta = 1.22\frac{\lambda}{D} \quad [\,\Theta\,] = \mathsf{rad} \qquad (2.2.1)$$

With a diameter of $100\,\mathrm{m}$ the Effelsberg Telescope[1] in Germany is one of the largest fully steerable radio telescopes in the world. Typical observations at $\lambda = 2\,\mathrm{cm}$, however, yield $\Theta_{Eff} \approx 50.33\,\mathsf{arcsecs}$ and are therefore not enough to analyze the desired core region of Mrk 421 for instance. The only way to improve $\Theta$ at a given wavelength is increasing $D$. Since construction of massive telescopes is limited and expensive, interferometry is used. Thereby, two or more telescopes are synchronized to simultaneously observe an object like one large telescope. The diameter then corresponds to the so called baseline which is the distance of two telescopes measured at the reflection center. For multiple dishes all over the world this is called Very Long Baseline Interferometry (VLBI). The longest baseline of the Very Long Baseline Array[2] (VLBA) for instance

---

[1] http://www.mpifr-bonn.mpg.de/effelsberg, 9. Feb 2018
[2] https://science.nrao.edu/facilities/vlba, 9. Feb 2019

counts $b \approx 8000\,\mathrm{km}$ achieving an angular resolution of $\Theta_{VLBA} \approx 0.59\,\mathrm{mas}$ at an observing wavelength of $\lambda = 2\,\mathrm{cm}$. Comparing this to $\Theta_{Eff}$ one can verify the benefits of radio interferometry.

## 2.2.2 Ideal Description

Taylor et al. (1999) describes how it is possible to synchronize two measurements based on the conclusions in Sect. 2.1. Essential for analyzing an observation at two distinct places is the correlation of the field at those locations $\boldsymbol{r_1}$ and $\boldsymbol{r_2}$. This is described by the coherence function $V_\nu$ expressed with

$$V_\nu(\boldsymbol{r_1}, \boldsymbol{r_2}) = \langle \boldsymbol{E_\nu}(\boldsymbol{r_1}), \boldsymbol{E_\nu^*}(\boldsymbol{r_2}) \rangle =$$

$$\left\langle \int dS_1 \int dS_2\, \varepsilon_\nu(\boldsymbol{R_1})\, \varepsilon_\nu^*(\boldsymbol{R_2}) \frac{e^{2\pi i \nu |\boldsymbol{R_1} - \boldsymbol{r_1}/c}}{|\boldsymbol{R_1} - \boldsymbol{r_1}|} \frac{e^{2\pi i \nu |\boldsymbol{R_2} - \boldsymbol{r_2}/c}}{|\boldsymbol{R_2} - \boldsymbol{r_2}|} \right\rangle . \tag{2.2.2}$$

Eq. 2.1.2 was utilized for the second expression and $*$ denotes the complex conjugate. The further simplification:

- The astronomical radiation is assumed to not be spatially coherent which causes $\varepsilon_\nu(\boldsymbol{R_1})\, \varepsilon_\nu^*(\boldsymbol{R_2})$ to be zero for $\boldsymbol{R_1} \neq \boldsymbol{R_2}$

yields $\boldsymbol{R_1} = \boldsymbol{R_1} = \boldsymbol{R}$. Introducing $\boldsymbol{s} = \boldsymbol{R}/|\boldsymbol{R}|$ the resulting absolute value $|\boldsymbol{R}|^2 \langle |\varepsilon_\nu(\boldsymbol{s})|^2 \rangle$ in Eq. 2.2.2 represents the observed intensity that will from now on be denoted with $I_\nu$. As mentioned in Sect. 2.1, the source is very far from the observer which justifies to neglect terms of order $|\boldsymbol{r}/\boldsymbol{R}|$ and allows to replace $dS$ with $|\boldsymbol{R}|^2 d\Omega$. Hereby the coherence function in Eq. 2.2.2 becomes

$$V_\nu(\boldsymbol{r_1}, \boldsymbol{r_2}) = \int I_\nu(\boldsymbol{s}) e^{2\pi i \nu \boldsymbol{s}(\boldsymbol{r_1} - \boldsymbol{r_2})/c} d\Omega. \tag{2.2.3}$$

This form, called spatial coherence function, clarifies that the coherence is only dependent on the relative distance which justifies using one reference point when operating with several telescopes. The last simplification:

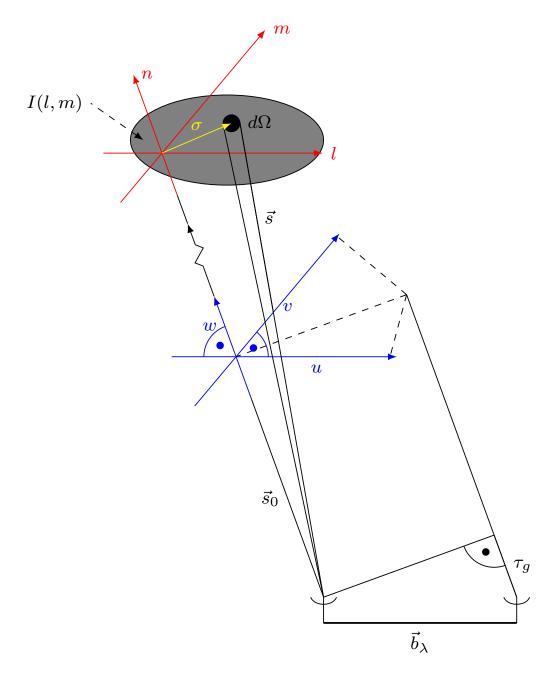- All radiation is expected to come from only a small portion of the celestial sphere.

**Figure 2.3:** Introduced coordinate systems based on the phase tracking center $s_0$. Intensity distribution of the source is thought to lay in the $(m, l)$-plane as described with $\sigma$. Telescopes lay in $(u, v)$-plane but for clarification shown this is shown with shift in sketch. (Figure adapted from Burd 2017)

implies that every location of the intensity $I_\nu$ on the sphere can be described with the location of the phase tracking center $\boldsymbol{s_0}$ and a perpendicular direction $\boldsymbol{\sigma}$ such that $\boldsymbol{s} = \boldsymbol{s_0} + \boldsymbol{\sigma}$. Based on this a coordinate system $(l, m, n)$ is introduced whereat $\boldsymbol{s_0} = (0, 0, 1)$ and $\boldsymbol{\sigma} = (\sigma_l, \sigma_m, 0)$ as shown in Fig. 2.3. The plane of $\boldsymbol{r_1} - \boldsymbol{r_2}$ in analogy can be conveniently described by the (u,v,w) coordinate system in units of wavelengths. In this coordinate transformation Eq. 2.2.3 reads:

$$V'_\nu(u, v, w) = e^{-2\pi i w} \int \int I_\nu(l, m) e^{-2\pi i (ul + vm)} \, dl \, dm \qquad (2.2.4)$$

Moving $e^{-2\pi i w}$ to the right side results in a $w$-independent left side which shows $V'_\nu(u, v, w) \, e^{2\pi i w} = V_\nu(u, v, w)$. The coherence function relative to the direction of the phase tracking center is therefore expressed by the Fourier transform of the intensity (also called brightness distribution).

$$V_\nu(u, v) = \int \int I_\nu(l, m) e^{-2\pi i (ul + vm)} \, dl \, dm \qquad (2.2.5)$$

$$V_\nu(u, v) \quad \xleftrightarrow{\text{FT}} \quad I_\nu(l, m)$$

Interferometers allow to measure this coherence function. By measuring the time delay $\tau_g$ with atomic clocks the telescope array can be synchronized to one reference antenna. This principle is technically possible for any electromagnetic wave but works better in practice for bigger wavelengths. Reason for this is the easier detectable interference pattern.

### 2.2.3 Real Measurement

In a real measurement, however, not all of the coherence function can be gathered which represents a loss of Fourier components. As an example for an obtained uv-coverage, a measurement analyzed in this study is shown in Fig. 2.5. Each trajectory represents the measurement for one baseline whereby the radial distance quantifies that distance. As the measurement is taken the earth keeps rotating and therefore more of the uv-plane is covered. The lack of information in the observed coherence function is taken into account with a sampling function $S(u, v)$. The corresponding Intensity $I_\nu^D$ for only some

points in the uv-plane is called dirty image.

$$I_\nu^D(l,m) = \int\int V_\nu(u,v)S(u,v)e^{2\pi i(ul+vm)}\,du\,dv \qquad (2.2.6)$$

The Fourier transform of the sampling function expressed with $B^D(l,m)$ is called the dirty beam[3] and allows to utilize the convolution theorem. This states that the product of two Fourier transforms (like $V_\nu(u,v)$ and $S(u,v)$) equals the Fourier transform of a convolution. Considering this the dirty image can be described as convolution (denoted with $\star$) of the desired intensity distribution and the dirty beam.

$$I_\nu^D(l,m) = I_\nu(l,m)\star B^D(l,m) \qquad \xleftrightarrow{\text{FT}} \qquad V_\nu(u,v)S(u,v) \qquad (2.2.7)$$

For reasonable analysis of the source it is essential to deconvolve this dirty image. That procedure will be outlined in Sect. 3.1.1.

While ideal observation assumes a point probe, antennas of real telescopes have finite extension. This is taken into account with the primary beam or normalized reception pattern $A_\nu(l,m)$ describing the sensitivity in each pointing direction. In analogy to above this can be added to the coherence function of Eq. 2.2.6 with the convolution theorem and the Fourier transform $B^P(u,v)$ of the primary beam.

$$A_\nu(l,m) = \int\int B^P(u,v)e^{2\pi i(ul+vm)}\,du\,dv \qquad (2.2.8)$$

The final resulting coherence function is usually referred to as the complex visibility function $V$ representing the convolution of the primary beam $B^P$ and the coherence function.

$$V(u,v) = \int\int A_\nu(l,m)I_\nu(l,m)e^{2\pi i(ul+vm)}\,dm\,dl \qquad (2.2.9)$$

$$V(u,v) = B^P(u,v)\star V_\nu(u,v) \qquad \xleftrightarrow{\text{FT}} \qquad A_\nu(l,m)I_\nu(l,m) \qquad (2.2.10)$$

This complex visibility is actually measured by arrays of radio telescopes. The next chapter will clarify how it is achieved to track back to the desired brightness distribution. Before the data can be analyzed it has to be calibrated. Hereby for example the measured amplitude has to be adjusted to flux density with a known calibration source. For VLBI

---

[3] $B^D$ is also called point-spread function or synthesized beam

this reduction can be conducted for instance with the Astronomical Image Processing System (AIPS). Since that progress is not part of this work, it will not be further discussed. A detailed description of the method can be found in Taylor et al. (1999)



**Figure 2.4:** Very Long Baseline Array and its individual antennas as presented on the National Radio Astronomy Observatory webpage[4].

---

[4]http://www.vlba.nrao.edu/sites/, 12. Feb 2018

## 2.3 Boston University Blazar Monitoring Program

The Boston University Blazar Monitoring Program[5] (BU) is a multiwavelength campaign observing bright $\gamma$-ray blazars as presented in Jorstad & Marscher (2016). Among other surveys the above introduced VLBA is used to analyze the kinematics of parsec-scale radio jets in 43 GHz. This telescope array consits of ten identical 25 m antennas in the northern hemisphere as shown in Fig. 2.4. The longest baseline counts 8000 km between Mauna Kea, Hawaii and St. Croix, Virgin Islands. Observations between 2.1 GHz and 96 GHz are possible. Further technical details can be found on the Long Baseline Observatory webpage[6]. In the context of the BU program 34 blazars are observed roughly every month in 8–10 scans of about 5 minutes with this array. That yields a total observation time of about 40 min and a rather sparse *uv*-coverage compared to other radio observations as can be seen in Fig. 2.5.

A summary of results regarding the kinematics of parsec-scale jets is given in Jorstad et al. (2017) including Mrk 421 (see Chap. 4). The authors support the theory of Jorstad et al. (2001) stating that strong $\gamma$-ray flares originate in the parsec-scale regions of a jet and can therefore be seen in mm wave images.

Based on those references the 43 GHz BU data is very suited for the scientific issue discussed in this work as clarified in Sect. 1.4. Therefore, the calibrated data for Mrk 421 provided on the BU homepage[7] from January 2012 to July 2013 covering 14 epochs will be analyzed.

Another additional epoch for the 19th of October 2012 was provided by the supervisor since this is very close to the flare. Also this measurement was taken with the VLBA at 43 GHz.

---

[5] https://www.bu.edu/blazars/VLBAproject.html, 5. Feb 2019
[6] https://science.lbo.us/facilities/vlba, 12. Feb 2018
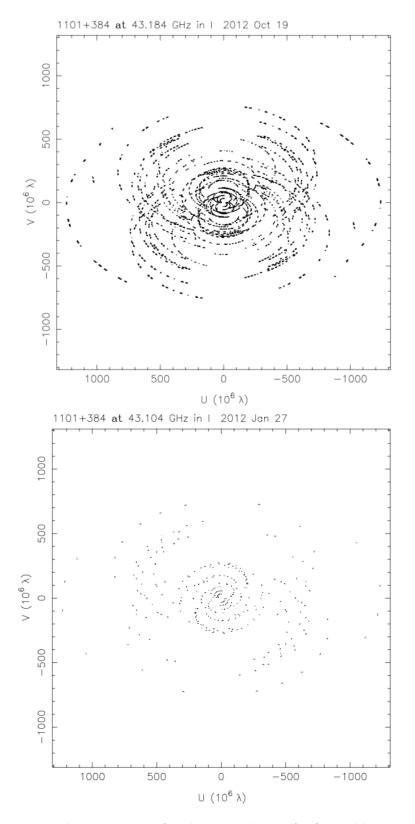[7] https://www.bu.edu/blazars/VLBA_GLAST/1101.html, 5. Feb 2019

**Figure 2.5:** Measured *uv*-coverage of Mrk 421 with VLBA after calibration. *Top:* Epoch 12/10/19 was provided by the supervisor. *Bottom:* Epoch 12/01/27 was part of BU as all other data and shows a more tenuous coverage due to shorter observation periods.

# 3 Data analysis

As pointed out in Sect. 2.2, the data obtained with radio interferometry represents the complex visibility function of Eq. 2.2.10. Fig. 2.5 *Top* shows the corresponding $uv$-plane for the observation on 12/10/19[1] after calibration. The $uv$-plot is obtained with the program difmap which was used for analysis of the BU data of Mrk 421 from January 2012 to July 2014 of this study. First this is achieved by deconvolution with the CLEAN algorithm and self-calibration. In a second approach the model-fitting technique is applied to analyze the data. The concerning results are presented here along with explanation of the methods and their assumptions while the interpretation and discussion is shown in Chap. 4.

## 3.1 Imaging

### 3.1.1 CLEAN algorithm

Aim of the CLEAN algorithm is to deconvolve Eq. 2.2.10 in order to constitute a map of the intensity. This so called clean map represents a model of the brightness distribution of the source and, therefore, allows to draw conclusions about its structure.

The concoction of the CLEAN algorithm can be found in Högbom (1974). Taylor et al. (1999) outlines the basic method and lists several available CLEAN algorithms and their procedure. This study will focus on the Högbom algorithm as used in difmap. Högbom (1974) explains how the dirty beam $B^D$ is adduced to identify real features of the source among noise from side lobes in an iterative process. To do so the brightest spots in the dirty map are specified by setting windows. The dirty map as well as $B^D$ are obtained by Fourier transformation of parameters from the measurement (see Sect. 2.2). The

---

[1] From here on all dates will be written in the format yy/mm/dd which corresponds to the 19th of October 2012 in this case.

CLEAN algorithm then fits point sources ($\delta$-peaks with no other background) to the data. Those peaks are multiplied with the mentioned dirty beam $B^D$ and subtracted from the dirty map at the corresponding position. The position and magnitude of all peaks is memorized while this step is iterated as long as peaks significantly brighter than noise are identified. The dirty map will eventually lack of features from the source and only contain even noise that is referred to as residuals. At this point the model with the gathered point sources is convolved with an idealized CLEAN beam $B^C$ resulting in a CLEAN map (or image) of the source. Hereby, $B^C$ is obtained by fitting an elliptical Gaussian to the central lobe of the dirty beam. Finally the residuals are added to the CLEAN map since this can reveal additional diagnostic information about the source.

### 3.1.2 Self-Calibration

As pointed out in Taylor et al. (1999) there are several calibration difficulties when observing with an interferometer. In order to interpret the data correctly those have to be taken into account. Clever design for instance allows to decrease significance of an additive offset. Eq. 3.1.1 clarifies the significant difference between the observed visibility $\widetilde{V}_{ij}$ and the true visibility $V_{ij}(t)$ for the i-j baseline.

$$\widetilde{V}_{ij}(t) = g_i(t)\, g_j^*(t)\, V_{ij}(t) + \epsilon ij(t) \tag{3.1.1}$$

Here, $g_i(t)$ and $g_j(t)$ denote the complex visibility gains[2] of the corresponding array element relative to one reference and $\epsilon(t)$ represents thermal noise. The gains are mainly caused by the above atmosphere and a smaller fraction originates within the antenna itself. The method of self-calibration is based on allowing those element gains to be free parameters. The aim is to receive a model of the intensity distribution $\widehat{I}_\nu$ based on the Fourier transform $\widehat{V}$ which equals the observed visibility with adjusted gain factors. Hereby $\widehat{I}_\nu$ is subject to restrictions that make this model astronomically plausible. Schwab (1980) constrains this with minimizing the sum of residuals $S_R$ by altering the gain factors $g_i(t)$ and $g_j(t)$ as well as the model intensity distribution $\widehat{I}_\nu$ (and thereby

---

[2] $g_i(t)$ and $g_j(t)$ are also called element gains or antenna gains

its FT $\widehat{V}$) according to:

$$S_R = \sum_k \sum_{\substack{i,j \\ i \neq j}} \omega_{i,j}(t_k)\, |\widetilde{V}_{ij}(t_k)\, -\, g_i(t_k)\, g_j^*(t_k)\, \widehat{V}_i j(t_k)|^2 \qquad (3.1.2)$$

The weighting factor $\omega_{i,j}(t_k)$ equals the reciprocal of the variance of $\epsilon_{ij}(t)$. Naturally this approach requires a lack of degrees of freedom in order to introduce a model $\widetilde{V}_{ij}(t)$. The method allows to refine a model in iterative steps whereby first of all there must be an initial model. This could for instance be obtained with CLEAN algorithm which, in combination, is called hybrid imaging. After the model is used to convert the source into a point source, Eq. 3.1.2 is adduced to solve for the complex gains. This yields a corrected visibility such that

$$V_{ij,corr}(t) = \frac{\widetilde{V}_{ij}(t)}{g_i(t_k)\, g_j^*(t_k)}. \qquad (3.1.3)$$

With this corrected data, a new model can be obtained. This steps are to be repeated as far as necessary.

All in all the explained methods work separately either utilizing the *uv*-plane (self-calibration) or the sky brightness (CLEAN algorithm). This eponymous "difference mapping" is used in the program difmap as introduced in Shepherd (1997). Difmap will be used to analyze the data in this study incorporating the methods explained above.

### 3.1.3 Imaging Results

Hybrid Imaging as explained above was used to build a CLEAN map for the epochs throughout 2012. As this study focuses on the kinematics of this source, the CLEAN maps were plotted according to their time evolution in Fig.3.1. The whole plot is rotated clockwise by 90 degrees which causes the northern direction of the maps to point to the right. The contour levels start at a value of $3\times$ noise level (obtained with difmap) and increase logarithmically.
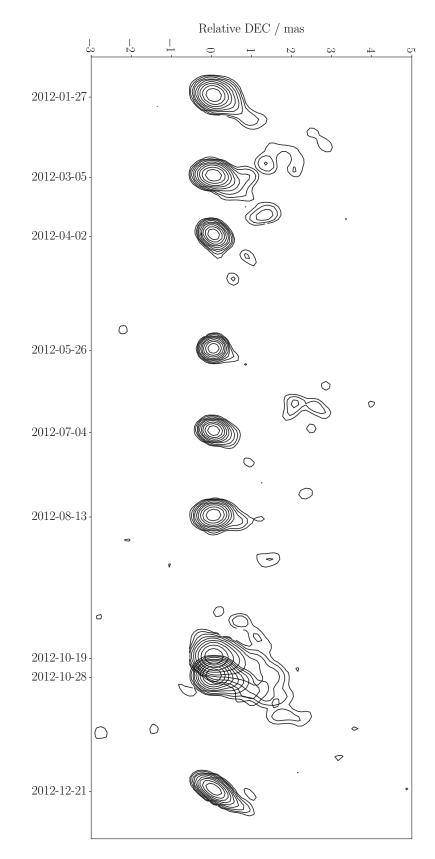
**Figure 3.1:** CLEAN maps obtained with difmap in chronological evolution.
Note: Figure is rotated clockwise by 90 degrees so right axis here points northwards.
Contour levels: Min = 3× noise level obtained with difmap, increasing logarithmically.

The images clearly show the dominant core that is aligned in each epoch. While the core is interpreted to stay put, knot-like components propagate along the jet axis as pointed out in Sect. 1.3. This result indicates that the jet emerges towards the upper right corner (North-West) of each epoch consistent with results from other studies (e.g. Richards et al. 2013; Lico et al. 2012). Nevertheless, the jet emission is very diffuse and it is not possible to identify single components that could be tracked in more than two epochs. The only feature present in almost all epochs is a bump in the contour lines very close to the core (circa 0.2 mas to 0.4 mas from the center) towards the jet direction. This could indeed indicate a rather stationary component close to the core. It is important to bear in mind the sparse $uv$-coverage obtained with the BU observations. This means that many of the Fourier components are unknown as only little of the complex visibility in the $uv$-plane is covered. A longer observation time as in 12/10/19 could have provided more information about the source. Based on this data the results do not allow to draw confident conclusions about the VLBI jet structure. Hence, another method will be used in the following to compare this findings.

## 3.2 Model-Fitting

### 3.2.1 Principle of Model-Fitting

As pointed out by Taylor et al. (1999) VLBI images of AGNs with jet emission often contain bright, isolated features. As shown in Sect. 1.3, those features are interpreted as components moving along the jet. It is useful to analyze the data based on such features since this enables comparison of observations of different frequencies. The components are hereby defined by their position, brightness (integrated intensity), size, and shape. Difmap allows to build a model of several components describing the source based on the dirty map. This approach is called model-fitting. To do so, one has to determine the location, shape (usually circular or elliptical) and size of a suspected component in the dirty map. In iterative steps this is then considered to be a Gaussian intensity distribution with the amplitude represented by the intensity of the component and a full width at half maximum (FWHM) given by the diameter of the component. Analogue to the CLEAN algorithm this Gaussian model is memorized while it is subtracted from the dirty map. Hereby, residuals representing remaining (unmodelled) emission appear

in the dirty map, which allow to fit further Gaussian components until no significant emission is left. The obtained model describes the brightness distribution of the source with Gaussian components.

## 3.2.2 Model-Fits for Mrk 421

The above explained procedure was conducted for the same nine epochs of 2012 as in Sec. 3.1.1 and another six epochs of 2013 from the BU website. Throughout the model-fitting process it became clear that the core was fitted best with two components. According to those models the core region is composed of a $\delta$-peak and one elliptical Gaussian component. While this is the best mathematical way to describe the data it is assumed that the physical reality does not show two distinct but only one feature. Bearing this in mind the two features will still be differentiated throughout the study. The $\delta$-peak was interpreted to be closest to the core and therefore assumed as stationary. The radial distance of all other components is measured in respect to this $\delta$-peak. As the components are thought to flow along the jet (see Sect. 1.3), they are expected to be seen at the same or a slightly further position in the map compared to the previous epoch. Hence, the relative radial distance can be used to identify a component throughout the epochs. This is best analyzed in the component evolution plot of Fig. 3.2 (bottom panel) where the relative distance of each component to the core is plotted along all epochs. Since this plot was only generated for identification purposes no error bars are included. The $\delta$ peak and the extended core component, shown as blue diamond and orange pentagon respectively, can be seen in every epoch apart from 12/12/21 which was best fitted with only one extended core component. Another component can be seen in relative distance of about 0.4 mas from the core as indicated with green triangles. However, it was not unambiguous to identify this component in every epoch. In this case it is indispensable to also compare the flux densities as shown in the top panel of Fig. 3.2. If those values do not vary significantly the epoch is interpreted to be the same. This criteria depicted the third component of epoch 12/08/13 to be different from the green component since the concerning flux densities were significantly below 0.02 mJy. This and other unidentified components are shown with purple hexagons. The third component of epoch 12/04/02 instead fitted with regard to the fluxes, even though it is very close to the core. It could be possible that this is another feature but for this
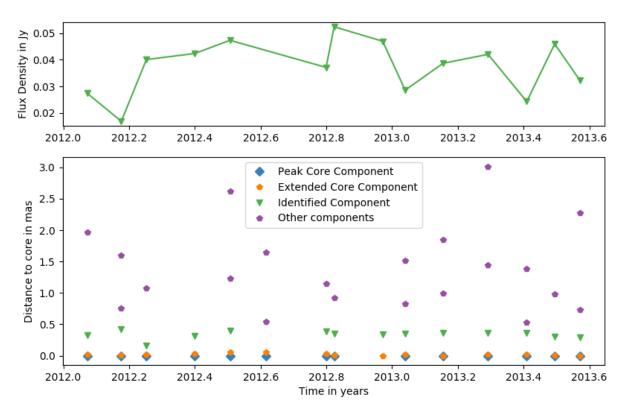
**Figure 3.2:** *Top*: Flux density evolution of only the green component. *Bottom*: Component evolution in Mrk 421 at 43 GHz obtained in difmap. Components are illustrated with characters explained in the legend.

study the component is treated equal to the other third components. At this point it is important to note that the models plotted in Fig. 3.2 were not single solutions. Several other schemes resulted for different settings in some cases while the third component of 12/04/02 for instance was always found at that spot. Based on the criteria listed above the most suitable models were chosen.

These models (colored circles representing components) are shown in in Fig. 3.3 aligned with the corresponding images (black contour plots representing flux density). In contrast to the 9 images of 2012 acquired in Sec. 3.1.1 with CLEAN algorithm, here six further epochs were included and the images were obtained with model-fitting. The results are shown chronologically along the x-axis of Fig. 3.3 divided on two pages. This allows to analyze the evolution of the VLBI jet structure throughout all epochs. The $\delta$-peak was again considered as stationary center and is shown in blue. The extended
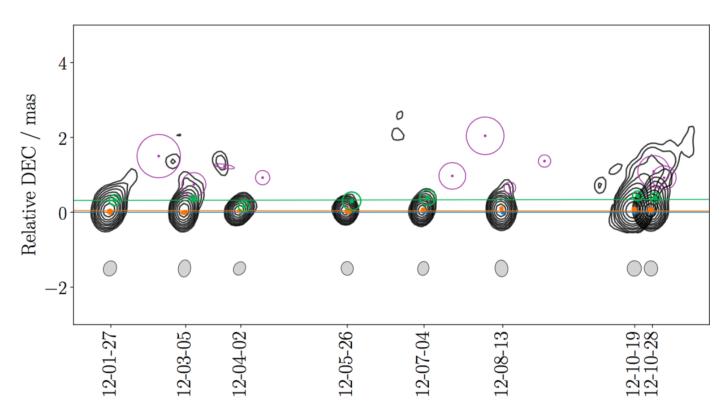
**Figure 3.3:** Model-fit components of Mrk 421 at 43 GHz on top of black brightness contour maps in chronological order from 12/01/27 to 12/10/28. Components are illustrated in blue (core peak), orange (extended core), green (identified) and purple (unidentified). Linear fits are shown for identified components (see Fig. 3.2).

elliptical core component is depicted with orange, the identified component with green and other components with purple in analogy to Fig. 3.2. The beam is shown in light grey underneath each concerning epoch. Linear fits are shown if identification of the component was possible according to Fig. 3.2 and the mentioned criteria. The fits were calculated in the initially continuous plot. Here, it is split on two pages in order to maintain the common notation of North pointing upwards and West pointing to the right. This causes an unproportional break between epoch 12/10/28 and 12/12/21. In other comparable studies (e.g. Jorstad et al. 2017) this methods yields more components. Often a better identification throughout the process is possible while during this analysis it was not clear where the components are located. Again only diffuse jet emission dominates the model. Apart from the core only one likely component at 0.4 mas
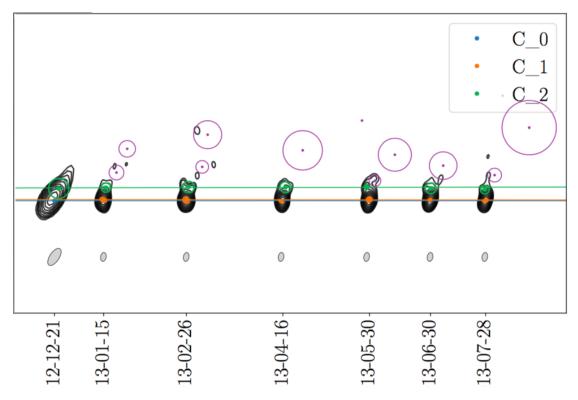
**Figure 3.3:** Continued from 12/12/21 to 13/07/28.

could be identified. This affirms the assumption made in Sec. 3.1.1. Nevertheless, also this method reveals difficulties. It is possible that the structure of the VLBI jet at such a high frequency (and therefore resolution) is too complicated to be described with Gaussian components.

### 3.2.3 Component Velocities

While the core is thought to be stationary it is possible to calculate the speed of the identified component with Fig. 3.4. In principle this is the same plot as Fig. 3.2, except only the identified components are shown. Furthermore, error bars for position uncertainty are shown defined by the size of the component (its radius). The uncertainties in time as in the observation date can be neglected in this representation. The speed of the identified component is given by the slope of its graph. As it is the simplest description, those speeds are assumed to be linear analogue to comparable studies (such as Piner &

Edwards 2018). Therefore, a linear regression in python was utilized to calculate the speed of the green component. In a first run the uncertainties of the data points were not taken into account which corresponds to an unbiased linear regression as shown in Fig. 3.2 resulting in:

$$v_{unb} = \frac{s}{t} = 0.0098 \pm 0.0373 \, \frac{\text{mas}}{\text{year}} \tag{3.2.1}$$

Afterwards a linear regression taking into account the uncertainties resulted in:

$$v_b = \frac{s}{t} = -0.0082 \pm 0.0323 \, \frac{\text{mas}}{\text{year}} \tag{3.2.2}$$

In the range of uncertainty, both speeds are in agreement with a steady component. This slow component speed is typical for blazars as pointed out in Piner & Edwards (2018).
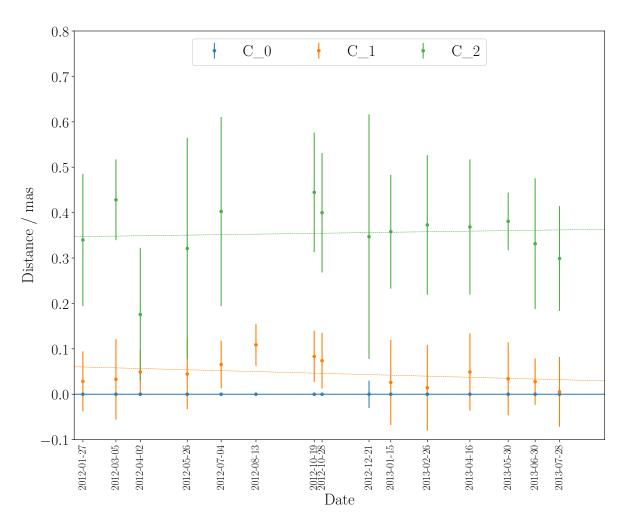
**Figure 3.4:** Evolution of only identified components in Mrk 421 at 43 GHz obtained in difmap with position uncertainties corresponding to the radius of the components. Fits are shown with unbiased linear regression.

# 4 Discussion

The analysis of 43 GHz data from Mrk 421 during 2012 and parts of 2013 shows that with the used methods the VLBI jet structure of this source can barely be modeled. The process rather leads to the conclusion that the method itself might not be applicable for that source. Nevertheless, there have been studies analyzing the very same data or data from before 2012. The following discussion will show that with the applied method the model-fitting is abiguous. Similarities and differences between this and previous studies will be elucidated. Further discussions concerning the observed flare in September 2012, Doppler factors, and a final summary of the results in this study will be presented.

## 4.1 Prior Kinematic Studies

### 4.1.1 Throughout 2011

Comparison of this study to a prior state is provided by Blasi et al. (2013). The analyzed 43 GHz data from a dedicated multi- frequency monitoring campaign and BU data throughout 2011. It will from now on be referred to as B2011. Hybrid imaging and model-fitting are used, analogue to this study. While on average six to seven Gaussian components were used to describe the surface brightness distribution of the source, four components could be identified in almost every epoch. Those are shown in Fig. 4.1 (*Top*) as adapted form B2011. The identification was based on relative distance to the core and flux density of each component as in this study. It appears striking that the model-fit method seems to work a lot better for the prior data. This, however, changes when not only the identified components but all components of the model-fits are included. Those can be found in Tab. 3 of B2011 and are plotted in Fig. 4.1 (*Bottom*). The comparison reveals that the interpretation of the deduced models is ambiguous. Identification gets rather unclear especially within the region of < 1 mas.
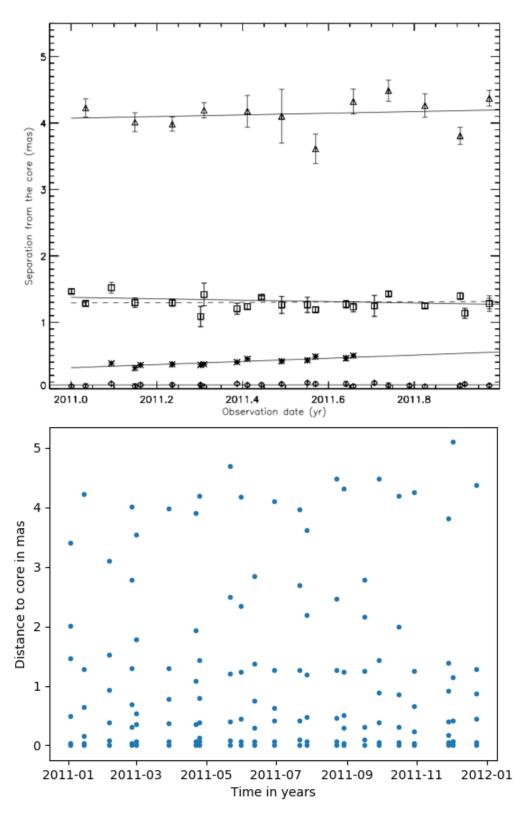
**Figure 4.1:** Component evolution of Mrk 421 obtained with model-fitting throughout 2011. *Top:* Figure published in Blasi et al. (2013) showing four clearly identified components. *Bottom:* All components found in Blasi et al. (2013) reveal that identification is ambiguous.

Bearing in mind that those components are not unambiguous, the results can still be used for comparison to this study. The innermost component of B2011 is found very close to the core ($< 0.1$ mas) and appears rather stationary. This could correspond to the extended core component of this study. The second component identified by B2011 appears from February to August and it is usually located at a core distance between 0.3 and 0.5 mas. The paper lacks of justification for the disappearance of that component while the obtained models do show several components at that distance with similar flux after August. It is stated that "components within 1 mas of the core are difficult to interpret and identify". This problem was faced in this study as well. If the model of B2011 is continued the second component should be found above 0.5 mas in the beginning of 2012 and up to around 1 mas by June 2013. This can not be confirmed with this study. It is possible that the detected second component in B2011 is not moving as rapid and therefore still found around 0.4 mas throughout 2012. This would imply that this component is stationary compared to components of other sources shown in Jorstad et al. (2017). The next component found in B2011 is located in a relative distance of about 1 mas from the core. This could not be reproduced in this study but some epochs do show emission in that area. The utmost identified component in B2011 can not be resolved in the BU data due to the lack of *uv*-coverage caused by the shorter duration of the observations.

In B2011 there were more observations of significant longer duration between an even shorter time frame compared to this work. It is shown that even with this circumstances the interpretation of Mrk 421 at 43 GHz is very complex. This particularly affects the central region of the jet which supports the result of this analysis. The innermost region of the jet appears too complicated to be described with Gaussian components which are tracked over time. One reason for this could be jet bending as mentioned in B2011. The prior model B2011 does show differences to this study but the found similarities remain constant. Therefore, no significant change respecting the flare of September 2012 in Mrk 421 could be detected.

## 4.1.2 From 2010 to 2012

The BU program is run by the Boston University Blazar Group. A summary of their own analysis can be found in Jorstad et al. (2017), hereafter J2017. 36 sources of the

campaign[1] have been analyzed in a total of 1929 images. The study aims to study the kinematics of parsec-scale jets in $\gamma$-ray blazars. Hereby a greater overview and general understanding are more in focus than source specific analysis. Nevertheless, there is a similar component evolution plot published for Mrk 421 that is presented here in Fig. 4.2 (*Top*). The most prominent feature is located in a distance of 0.4 mas from the center in accordance to B2011 and this study. It is further mentioned that also the utmost component in J2017 can be associated with the feature right above 1 mas in B2011. The fact that this component appears to be moving inwards in J2017 is not further discussed. The rapidly moving component B2 (see Fig. 4.2) is thought to be ejected during high activity and correlated variability at X-ray and TeV energies (see Aleksić et al. 2015). The most striking feature is component B1 (see Fig. 4.2) that appears to be ejected in 2010. It is stated that the component all in all is doubtful since it is not detected at a lager distance than 0.5 mas anymore.

A new component like B1 or B2 would be expected in aftermath of the flare in September 2012 and the $\gamma$-flare according to Jorstad et al. (2001). However, just like in this work, no new component was detected. In J2017 it is mentioned that a new knot associated with the strong $\gamma$-ray outburst could be seen in the last epoch 13/01/15 of that study. This can not be confirmed within this study with epochs up to 13/07/28. The absence of a new component in J2017 as well as this independent study lead to the conclusion that the flare did not affect the VLBI jet structure within the time of observation.

In analogy to the analysis of B2011 not only the identified but also all other components for Mrk 421 are plotted in Fig. 4.2 *bottom*. The corresponding models can be found on the website of the HTML version of J2017[2]. Also in this comparison it becomes clear how ambiguous the models obtained with model-fitting (Gaussian components) are. They underlie a process of interpretation that can be very complex such as flux comparison, comparison to other epochs, and comparison to other scales. The VLBI jet structure of the source Mrk 421 proves to be rather complicated especially in the region within 1 mas.

---

[1] 21 quasars, 12 BL Lacertae objects (BLLacs) and 3 radio galaxies

[2] http://iopscience.iop.org/0004-637X/846/2/98/suppdata/apjaa8407t2_mrt.txt, 20. Feb '18
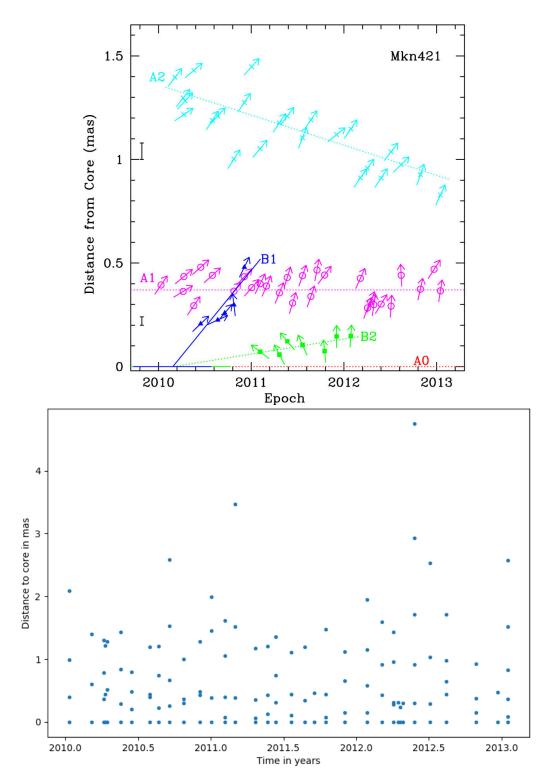
**Figure 4.2:** Component evolution of Mrk 421 obtained with model-fitting from 2010-2012. *Top:* Figure published in Jorstad et al. (2017) showing four clearly identified components A1, A2, B1, B2 and the core A0. *Bottom:* All components found online in the HTML version of Jorstad et al. (2017).

The prior discussed publications show that the utilized methos may be unsufficient when adapting them to a blazar with a complex structure like Mrk 421. This accounts especially for model-fitting the innermost jet close to the core and the core region itself with two-dimensional Gaussians. Nevertheless, when using this method one has to bear in mind the uncertainty of the components. Comparing results in J2017 to this study clarifies how subjective the model-fitting method is. With exactly the same data and the same method two individual models emerge for each epoch. This fact alone puts high constrains on the universal validity of this method in this case.

## 4.2  Doppler Factors and Doppler Crisis

As introduced in Sect.1.2 the Doppler Factor $\delta$ is now calculated based on the results of this kinematics study. The the obtained speed $v_{unb} = (0.0098 \pm 0.0373)\,\mathsf{mas/year}$ is chosen for this and will from here on be denoted with $v$. This determines $\beta_{app} = (0.6 \pm -2.2)^{-11} \times c$, $\beta = (0.7 \pm 2.59)^{-11}$ and $\gamma = \frac{1}{\sqrt{1-\beta^2}} \approx 1$. The inclination angle is approximated with $\theta = (15 \pm 10)°$ as typical for such objects. According to Eq. 1.2.12 those values yield the the Doppler factor

$$\delta = \frac{1}{\gamma(1 - \beta\cos(\theta))} \approx 1 \tag{4.2.1}$$

This modest value is lower than resulting Doppler factors of other studies like Richards et al. (2013) and Lico et al. (2012) where the calculation was also based on VLBI data. The discrepancy tracks back to the fact that the utilized method for identifying the components that hold the used velocity is ambiguous for the 43 GHz data. Since all resulting models were difficult to interpret, the latter study took into account a range of possible values. For $0.82 < \beta < 1$ and $0° < \theta < 35.0°$ Doppler factors were given to be $\delta < 20, 10, 5, 3$ for $\theta > 3.0°, 5.7°, 11.5°, 19.4°$ respectively. This shows the high range of uncertainty in that way of calculation.

Another approach to study this Doppler factor is provided in high energy observations. Those conclude that the value should be a lot bigger than VLBI observations suggest. While Maraschi et al. (1999) predict $\delta > 10$, Aleksić et al. (2012) even obtain $40 < \delta < 80$. That big discrepancy of Doppler factors is not understood yet and therefore called

Doppler crisis. There are models that suggest a velocity structure within the jet that could explain this differences (see Piner & Edwards 2013).

## 4.3 Light Curve

In order to analyze the flare of Mrk 421 from September 2012 in 43 GHz in particular, another light curve similar to Fig. 1.7 is obtained. That figure published in Richards et al. (2013) incorporates two data points for 43 GHz as illustrated with purple lines which is not enough to draw conclusions like a flare out of it. For this purpose the flux density of the core throughout the time observed in this study is shown in Fig. 4.3 in green. This is composed of the sum of the flux densities of the core components ($\delta$-peak and elliptical extended component as shown in Fig. 3.2). Error bars are dismissed in this presentation. Even this set of data points does not allow to draw confident conclusions about the behavior of the graph. In consequence more data points were incorporated from the BU website. The intensity-peaks for each epoch were added to the graph in Fig. 4.3 in blue. As this does not include the flux of the whole core there is a systematic offset between the data sets. The crucial behavior, however, is similar. The graph does not show the expected sharp peak as presented in Richards et al. (2013) for other frequencies. In that study it is elucidated that a pre-flare can be seen around mid of August 2012 (indicated with an yellow vertical line) in some frequencies and an extraordinary multiwavelenght flare takes places during September 2012 (shown with a red vertical line) as pointed out in Sec.1.4. Other than expected none of those flares shows up at 43 GHz based on this data. Instead, the flux density seems to increase steadily from the time of the flare on. By July 2013 it seems like the graph decreases again. This could be interpreted as a seperate flare in early 2013. Nevertehless, it could also be possible that the component that is expected to be ejected in aftermath of the September 2012 flare moves so slow that it only becomes distinguishable at that point. This could be analyzed in future studies. The assumption, however, is very doubtful since the light curve in Richards et al. (2013) does show the flare in even higher frequencies like 86 and 143 GHz.
Another explanation for the different shapes of the light curves could be that Fig. 1.7 and the radio data of Fig. 4.4 are based on the flux density of the whole source while Fig. 4.3 only shows core (or peak) emission. Lack of the flare in the latter could indicate
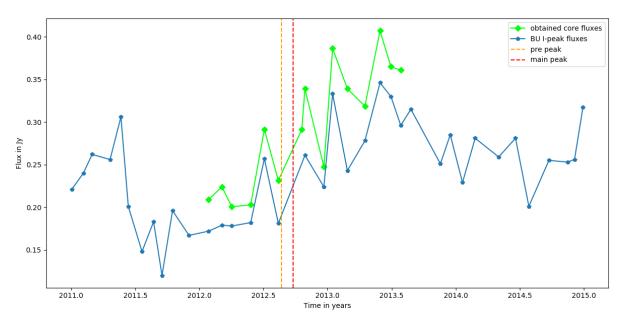
**Figure 4.3:** Light curve of core flux density of this study (green) and intensity peak
according to BU (blue) of Mrk 421. Richards et al. (2013) reports a pre-flare in Au-
gust 2012 (yellow) at some frequencies and an extraordinary multiwavelength flare in
September 2012 (red)

that it was caused in a further outward region of the jet. This is, however, unlikely
based on the fact that most of the emission is found in the core region.

As pointed out in Sect. 1.4 the connection to $\gamma$-ray flaring caused particular interest in
the extreme event studied here. Hovatta et al. (2015) discusses the correlation of the
radio flare and the two prior $\gamma$-ray peakes. To do so Fermi LAT ($\gamma$-ray), OVRO (15 GHz),
Metsähovi (39 GHz), and CARMA (95 GHz) data (as shown in Fig. 4.4) is utilized to draw
conclusions. Based on another flare in early 2013 a one-zone synchrotron self-Compton
(SSC) model was fitted to estimate the parameters of the emission region. With this
framework the radio flare of 2012 could either be connected with the first $\gamma$-ray peak
and a varying Doppler factor or with the second one and strong magnetic fields. It
becomes clear that both scenarios are subject to a very specific choice of parameters.
This confirms the unique and extreme nature of the event. That could also account for
a different reason of the flare than the ejection of a new component in the core region.
Comparing those light curves in Fig. 4.4 to Fig. 4.3 confirms that in contrast to other
wavelengths the 43 GHz data do not allow to distinguish the flare of 2012 from usual
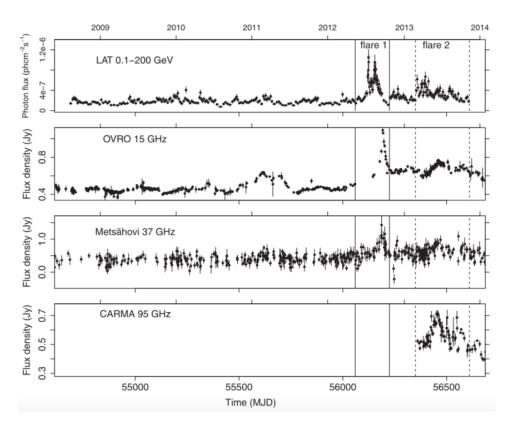
**Figure 4.4:** From top to bottom: light curves of Mrk 421 in γ-rays from Fermi LAT, radio 15 GHz from OVRO, 37 GHz from Metsahovi, and 95 GHz from CARMA. The solid lines indicate the time range for the 2012 flare and the dashed lines indicate the time range for the 2013 flare. (Figure adapted from Hovatta et al. 2015)

behavior. The second flare in 2013, however, does also show up in this wavelength.

## 4.4  Conclusions of this Kinematic Study

Hybrid imaging and model-fitting has proven to be suited very well for describing Mrk 421 in differend wavelenghts (see Richards et al. 2013 and Lico et al. 2012) as well as for other sources at 43 GHz (see Jorstad et al. 2017). Nevertheless, the BU data from January 2012 up to July 2013 allow to set only poor constrains on the jet structure here. Facing the results of this study, no impact of the radio flare in September 2012 can be seen in the VLBI jet structure at 43 GHz. The structure of the source seems

to be completely unaffected by the flare and does not change throughout the critical period of observation. The light curve, however, leads to the conclusion that a new component could have been ejected in Summer 2013 but the correlation to the flare in September 2012 becomes weaker for such a long delay. Another explanation is that the flare of September 2012 was caused by a another event than the ejection of a new radio component.

This is, however, not a comprehensive conclusion. Due to the fact that the utilized methods of hybrid imaging and model-fitting only yield poor results it is vague to draw conclusions out of those. This does not only hold for this but also the previous studies on Mrk 421 in 43 GHz (see Fig. 4.1 and Fig. 4.2). Considering this it is also possible that those methods are not suitable for Mrk 421. The CLEAN method does not yield enough information to analyze the jet structure. The model-fitting procedure represents - with only two-dimensional round or elliptical Gaussian components in the jet - one of the simplest possible interpretations. It is easily conceivable that Mrk 421 incorporates a more complex structure that can not be represented with such models. The findings of this study might also indicate that the well established model derived in Marscher & Gear (1985) is not well applicable to this source. This would suggest a more complex model or even a different explanation. Hence, further studies about the VLBI jet structure of Mrk 421 are crucial to get a better understanding of such sources and their mechanisms. A good *uv*-coverage is essential for future observations in order to put higher constrains on the quality of the modeling methods.

# Bibliography

Abdo A.A., Ackermann M., Agudo I., et al., 2010, ApJ 716, 30

Abdo A.A., Ackermann M., Ajello M., et al., 2011, ApJ 736, 131

Ackermann M., Ajello M., Allafort A., et al., 2011, ApJ 743, 171

Aleksić J., Alvarez E.A., Antonelli L.A., et al., 2012, A&A 542, A100

Aleksić J., Ansoldi S., Antonelli L.A., et al., 2015, A&A 576, A126

Blandford R.D., Payne D.G., 1982, MNRAS 199, 883

Blandford R.D., Znajek R.L., 1977, MNRAS 179, 433

Blasi M.G., Lico R., Giroletti M., et al., 2013, A&A 559, A75

Boccardi B., Krichbaum T.P., Ros E., Zensus J.A., 2017, Astonomy and Astrophysics Reviews 25, 4

Burd P.R., 2017, Masterthesis, Julius-Maximilians-Universitaet Wuerzburg

Burke B., Graham-Smith F., 2010, An Introduction to Radio Astronomy, Cambridge University Press

Cohen M.H., Lister M.L., Homan D.C., et al., 2007, ApJ 658, 232

D'Ammando F., Orienti M., 2012, The Astronomer's Telegram 4261

Gaidos J.A., Akerlof C.W., Biller S., et al., 1996, Nat 383, 319

Högbom J.A., 1974, Astron. Astrophys. Suppl. 15, 417

Hovatta T., Petropoulou M., Richards J.L., et al., 2015, MNRAS 448, 3121

Hovatta T., Richards J.L., Aller M.F., et al., 2012, The Astronomer's Telegram 4451

Hovatta T., Valtaoja E., Tornikoski M., Lähteenmäki A., 2009, A&A 494, 527

Jorstad S., Marscher A., 2016, Galaxies

Jorstad S.G., Marscher A.P., Mattox J.R., et al., 2001, The Astrophysical Journal 556, 738

Jorstad S.G., Marscher A.P., Morozova D.A., et al., 2017, ApJ 846, 98

Kadler M., 2017, Lecture: Multiwavelength Astronomy - Extragalactic Jets

Kellermann K.I., Sramek R., Schmidt M., et al., 1989, AJ 98, 1195

Lico R., Giroletti M., Orienti M., et al., 2012, A&A 545, A117

Mannheim K., 1993, A&A 269, 67

Maraschi L., Fossati G., Tavecchio F., et al., 1999, ApJL 526, L81

Marscher A.P., Gear W.K., 1985, ApJ 298, 114

Paggi A., Massaro F., Vittorini V., et al., 2009, A&A 504, 821

Piner B.G., Edwards P.G., 2013, In: European Physical Journal Web of Conferences, Vol. 61. European Physical Journal Web of Conferences, p. 04021

Piner B.G., Edwards P.G., 2018, ApJ 853, 68

Punch M., Akerlof C.W., Cawley M.F., et al., 1992, Nat 358, 477

Richards J.L., Hovatta T., Lister M.L., et al., 2013, In: European Physical Journal Web of Conferences, Vol. 61. European Physical Journal Web of Conferences, p. 04010

Rybicki G.B., Lightman A.P., 1986, Radiative Processes in Astrophysics

Schmitt J.L., 1968, Nat 218, 663

Schwab F.R., 1980, In: Rhodes W.T. (ed.) 1980 International Optical Computing Conference I, Vol. 231., p.18

Shakura N.I., Sunyaev R.A., 1973, A&A 24, 337

Shepherd M.C., 1997, In: Hunt G., Payne H. (eds.) Astronomical Data Analysis Software and Systems VI, Vol. 125. Astronomical Society of the Pacific Conference Series, p. 77

Strittmatter P.A., Serkowski K., Carswell R., et al., 1972, ApJL 175, L7

Taylor G.B., Carilli C.L., Perley R.A., 1999, In: Taylor G.B., Carilli C.L., Perley R.A. (eds.) Synthesis Imaging in Radio Astronomy II, Vol. 180. Astronomical Society of the Pacific Conference Series

Urry C.M., Padovani P., 1995, PASP 107, 803

Urry C.M., Scarpa R., O'Dowd M., et al., 2000, ApJ 532, 816

Vermeulen R.C., Ogle P.M., Tran H.D., et al., 1995, ApJL 452, L5

Verschuur G., 2007, The Invisible Universe - The Story of Radio Astronomy

# Acknowledgments

Finally I would like to thank all the people who helped me to write this thesis and to build up solid knowledge of studying blazars with radio astronomy.

First of all I want to express my gratitude towards Matthias Kadler. He did not only support my thesis but also gave me the possibility to include an ERASMUS exchange into my bachelors studies where I could prepare for it. Throughout all this time he always had an open ear (and skype account) for scientific questions, discussions and bureaucratic difficulties. Only with his contribution and the support of Jean Geurts I had the chance to study abroad which was eye-opening with regard to scientific work and also personal development.

Furthermore my ERASMUS semester in Turku, Finland, and this thesis were supported by Talvikki Hovatta. Being in a new country and culture she supported me whenever I needed help or advise and included me into the lovely work group at Tuorla Observatory. I am grateful to her for the time we spent discussing science and I value everything l learned in Turku about Astronomy.

I consider myself very lucky to call Paul Ray Burd my mentor. Ever since his tutorials in the beginnings of my studies he inspired me to work hard in order to reach my goals. Also today I look up to him and I am very thankful for his support. Having him next door to my office is absolutely valuable and really amusing especially in connection with Jonas Ringholz and Michael Seeg.

In addition I want to thank all other members of the chair of astronomy who integrated me without hesitation and always were open for discussions.

I appreciate the support of my parents Günter and Brigitte who gave me the possibility and strength to study here in Würzburg and the will to fulfill my dreams. I thank my brother Rendl who always brings me down to earth and makes me laugh however bad the situation might be. At last I want to thank my sweetheat Tobias for his love and always being there for me no matter what.

---

[3] VLBA-BU-BLAZAR http://www.bu.edu/blazars/VLBAproject.html

# Declaration

I, Sarah Wagner, declare that this thesis titled, 'VLBI Jet Kinematics of Mrk 421 concerning the Radio Flare in 2012' and the work presented in it are my own. I confirm that:

- This work was done wholly or mainly while in candidature for a research degree at this University.

- Where any part of this thesis has previously been submitted for a degree or any other qualification at this University or any other institution, this has been clearly stated.

- Where I have consulted the published work of others, this is always clearly attributed.

- Where I have quoted from the work of others, the source is always given. With the exception of such quotations, this thesis is entirely my own work.

- I have acknowledged all main sources of help.

- Where the thesis is based on work done by myself jointly with others, I have made clear exactly what was done by others and what I have contributed myself.

Signed:
_____

Date:
_____